Bio-Design and Manufacturing (2025) 8:524–542
https://doi.org/10.1631/bdm.2400436

RESEARCH ARTICLE

Ultrasmall ruthenium nanoparticles with enhanced and tunable multienzyme-like activity for periodontitis treatment

Yangjie Shao[1,2] · Pengpeng Xue[3] · Dongqi You[1,2] · Mingjian Zhu[3] · Zhouyang Qian[1,2] · Bo Zhang[4] · Shanbiao Liu[3] · Peihua Lin[4,5] · Zhichao Liu[1,2] · Chaoying Zhang[1,2] · Xinyue Hu[1,2] · Yuan Xie[1,2] · Menghan Xu[1,2] · Daishun Ling[4] · Fangyuan Li[5] · Mengfei Yu[1,2]

Received: 28 October 2024 / Accepted: 26 February 2025

Abstract

Periodontitis is an inflammatory disease caused by oxidative stress and initiated by bacterial infection. The endogenous enzyme system is dysfunctional in the periodontitis microenvironment. Currently, traditional clinical treatment cannot efficiently eliminate bacteria or relieve inflammation. To address this issue, we developed ultrasmall ruthenium nanoparticles (US-RuNPs) with multienzyme-like activity. Our results indicated that US-RuNPs with an amplified electric field had a superior photothermal effect to large-sized RuNPs. Thus, US-RuNPs, through photothermal therapy (PTT), acted as "bacterial lysozyme" to eliminate planktonic pathogens and biofilms. In addition, the antioxidant enzyme-like activity of US-RuNPs was greater than that of large-sized RuNPs, and US-RuNPs could scavenge intracellular reactive oxygen species (ROS) and inhibit inflammation-related responses. More importantly, US-RuNPs demonstrated a satisfactory effect against periodontitis in vivo due to their synergistic antibacterial activity through PTT and antioxidant effects even in deep sites, decreasing the alveolar bone loss to root length ratio (ABL/RL) from 70.70% to 20.15% and increasing the collagen volume fraction from 16.88% to 57.64%. Thus, US-RuNPs with approximately 2 nm diameter, mimicking multienzyme activity, have great potential for the treatment of periodontitis.

Yangjie Shao, Pengpeng Xue, and Dongqi You have contributed equally to this work.

✉ Daishun Ling
dsling@sjtu.edu.cn

✉ Fangyuan Li
lfy@shsmu.edu.cn

✉ Mengfei Yu
yumengfei@zju.edu.cn

[1] The Affiliated Hospital of Stomatology, School of Stomatology, Zhejiang University School of Medicine, Hangzhou 310006, China

[2] Key Laboratory of Oral Biomedical Research of Zhejiang Province, Hangzhou 310006, China

[3] Institute of Pharmaceutics, College of Pharmaceutical Sciences, Zhejiang University, Hangzhou 310058, China

[4] Frontiers Science Center for Transformative Molecules, School of Chemistry and Chemical Engineering, School of Biomedical Engineering, National Center for Translational Medicine, State Key Laboratory of Oncogenes and Related Genes, Shanghai Jiao Tong University, Shanghai 200240, China

[5] Songjiang Research Institute and Songjiang Hospital, Shanghai Key Laboratory of Emotions and Affective Disorders (LEAD), Shanghai Jiao Tong University School of Medicine, Shanghai 200025, China

Graphical abstract

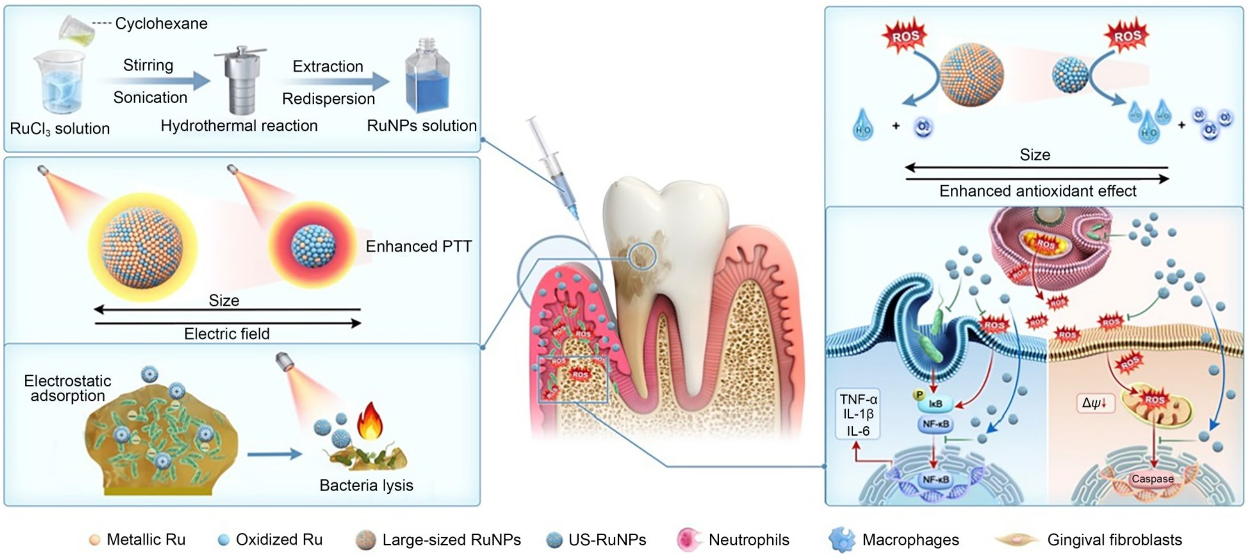

Keywords Ruthenium nanoparticles · Ultrasmall · Nanozymes · Photothermal therapy · Bacterial infection · Oxidative stress

1 Introduction

Periodontitis is a chronic inflammatory disease of periodontal supporting tissues caused by local stimulation from dental plaque, occlusal trauma, and other local irritants [1, 2]. Over 10% of adults are affected by severe periodontal disease, making it the 6th most common disease worldwide [3]. Importantly, periodontitis not only affects oral health, inducing swollen gums, gingival bleeding, formation of periodontal pockets, and tooth loss, but is also closely related to the development of Alzheimer's disease, cardiovascular disease, diabetes, rheumatoid arthritis, and other systemic diseases [4, 5].

Bacterial infection is the initial factor for periodontitis occurrence [6]. On the one hand, pathogenic bacteria secrete virulence factors to damage cells [7]. On the other hand, they gather with other microorganisms to promote the formation of plaque biofilms, which act as barriers to mechanical and antibiotic therapy [8, 9]. Next, pathogens may enter the systemic circulation through the periodontal tissues, affecting the whole body [10, 11]. In addition, bacteria hyperactivate multinucleated neutrophils, triggering excessive reactive oxygen species (ROS) production. Under physiological conditions, ROS can be maintained at an appropriate concentration by the endogenous enzyme system. However, endogenous enzymes might become unstable and denature in the periodontitis microenvironment, leading to ROS accumulation [12]. The imbalance between the endogenous enzyme system and ROS levels exacerbates inflammatory responses [13, 14]. Inflammatory cytokines secreted by neutrophils, macrophages, monocytes, and natural killer (NK) cells participate in the pathogenesis of periodontitis and may contribute to patient susceptibility [15–17]. Similarly, ROS dysregulation promotes osteoclast differentiation by activating nuclear factor-kappa B and mitogen-activated protein kinases, causing alveolar bone resorption in periodontitis [18, 19]. Therefore, bacterial elimination and ROS scavenging are key to periodontitis therapy.

In the clinic, scaling and root planning (SRP) is the principal approach to treating periodontitis. However, these mechanical therapies are not ideal. First, the dental instruments can hardly reach deep periodontal pockets or root bifurcations [20]. Residual periodontal pockets provide a favorable environment for the regrowth of pathogens, thereby compromising treatment efficacy. Although surgical interventions might deal with deep periodontal pockets, surgical therapy increases the anxiety, pain, and economic burden on patients. Moreover, both SRP and surgical therapy are technically demanding and require high levels of expertise [21]. In addition, SRP demonstrates limited efficacy in modulating host inflammatory responses, through which ROS subsequently induce tissue damage. Oral administration of antibiotics and anti-inflammatory drugs not only results in low drug concentrations in the periodontal pockets but also easily leads to the emergence of drug-resistant bacteria, adverse gastrointestinal reactions, and systemic immune disorders [22, 23]. In Table S1 (supplementary information), we show current common periodontitis treatments, which are limited in terms of efficacy and procedures. Thus, there is a need for a more efficient method to treat periodontitis.

Nanozymes have the advantages of local delivery and minimally invasive administration, showing great promise for periodontal applications. Compared to natural enzymes, nanozymes can tolerate the harsh microenvironment of periodontitis, reduce production costs, and have catalytic activity surpassing that of natural enzymes [24]. For example, ceria-based nanozymes show catalytic activity similar to catalase (CAT), superoxide dismutase (SOD), and peroxidase. Therefore, they can scavenge ROS and relieve tissue inflammation [25, 26]. To satisfy both antibacterial and anti-inflammatory demands for periodontitis therapy, multifunctional nanozymes are the current trend. However, although nanozymes can be modified to enhance functionalities, for example, through the design of bi-metallic nanozymes and multicomponent nanomaterials, the addition of various elements may increase biotoxicity [27].

Ruthenium (Ru) is a transition metal in group 8. Recently, Ru nanozymes have shown several attractive features in the biomedical field. First, Ru is a redox-active element and Ru nanozymes exhibit efficient interconversion between redox couples, which endows Ru nanozymes with antioxidant enzyme-like activity to scavenge ROS [28, 29]. Recent studies reported that Ru nanozymes could be used for the prevention and treatment of oxidative stress-related diseases such as acute kidney injury and central post-stroke pain [30, 31]. Moreover, Ru nanozymes have satisfactory biosafety. Liu et al. proved the biosafety of Ru nanozymes in vivo after long-term therapy [30]. Wu et al. found that the cell viability was unaffected at concentrations of Ru nanozymes up to 1.2 mg/mL [32]. Although some nanomedicines exhibit undesirable interactions with red blood cells, Ru nanozymes failed to cause evident hemolysis [31]. In addition, Ru nanozymes can be used as photothermal agents (PTAs) to remove bacteria through photothermal therapy (PTT) [33–35]. In particular, Ru nanozymes with positive charges can selectively bind to bacteria with negative charges [36]. Then, under laser irradiation, they break up cell walls and denature biomacromolecules. This bactericidal process is like that of phage lysozyme, which specifically recognizes the bacterial cell wall and degrades peptidoglycan, thereby causing bacterial lysis and death [37]. Thus, we refer to this PTT activity of Ru nanozymes as "bacterial lysozyme-like activity." This antibacterial method shows broad-spectrum antimicrobial activity, prevents the formation of plaque biofilms, and decreases the potential of bacterial resistance [38]. Despite concerns about heat damage to the nearby tissues caused by PTT, there are promising approaches to reducing side effects such as developing PTAs with specific interaction with bacteria, controlling irradiation parameters, and combining PTT with other antibacterial therapies [39–41].

Although Ru nanozymes exhibit many advantageous properties, the efficient delivery of nanozymes to the target sites is key to clinical success. Tissues containing complex structures with significant depth may impede nanozyme accumulation around target sites, decreasing drug efficacy [42]. Nanozyme size greatly influences drug transport. The preferred size for intravenous injection is 2–200 nm [43]. Although larger nanozymes can avoid being filtered out from the bloodstream by the kidneys, smaller nanozymes are more advantageous for tissue penetration [44]. Furthermore, the enzyme-like activity of nanozymes in the form of nanoparticles is substantially improved by decreasing their size [45]. Based on the above, we developed ultrasmall ruthenium nanoparticles (US-RuNPs) as nanozymes with a diameter of approximately 2 nm. US-RuNPs had better multienzyme-like activity than large-sized RuNPs. We proved that under near-infrared (NIR) laser irradiation, US-RuNPs could fight against *Fusobacterium nucleatum* (*F. nucleatum*) and *Porphyromonas gingivalis* (*P. gingivalis*) effectively. Further, US-RuNPs exhibited a protective effect on cells under oxidative stress. Then, a rat model of periodontitis was used to investigate the therapeutic effect of US-RuNPs in vivo. Given their ultrasmall size and electrostatic adsorption to bacterial surfaces, US-RuNPs could be delivered into deep sites of periodontal pockets, and decrease bacterial colonization through PTT. Furthermore, US-RuNPs regulated the immune microenvironment through continuous ROS scavenging and promoted the regeneration of periodontal tissues. Overall, our research suggests that US-RuNPs are potential therapeutic agents for periodontitis.

2 Results

2.1 Preparation of US-RuNPs

First, US-RuNPs with a diameter of approximately 2 nm were synthesized using an emulsion-based solvothermal method (Fig. 1a). Subsequently, X-ray diffraction (XRD) analysis was carried out to investigate the chemical composition of US-RuNPs. Data were analyzed in comparison with the standard card for RuO_2 (PDF #43-1027) from the powder diffraction file (PDF) database provided by the International Center for Diffraction Data, indicating the presence of RuO_2 peaks in US-RuNPs (Fig. 1b). X-ray photoelectron spectroscopy (XPS) analysis indicated that US-RuNPs were composed primarily of oxidized Ru, which constituted over 90% of the composition (Fig. 1c; Fig. S1a in the supplementary information). To further evaluate the

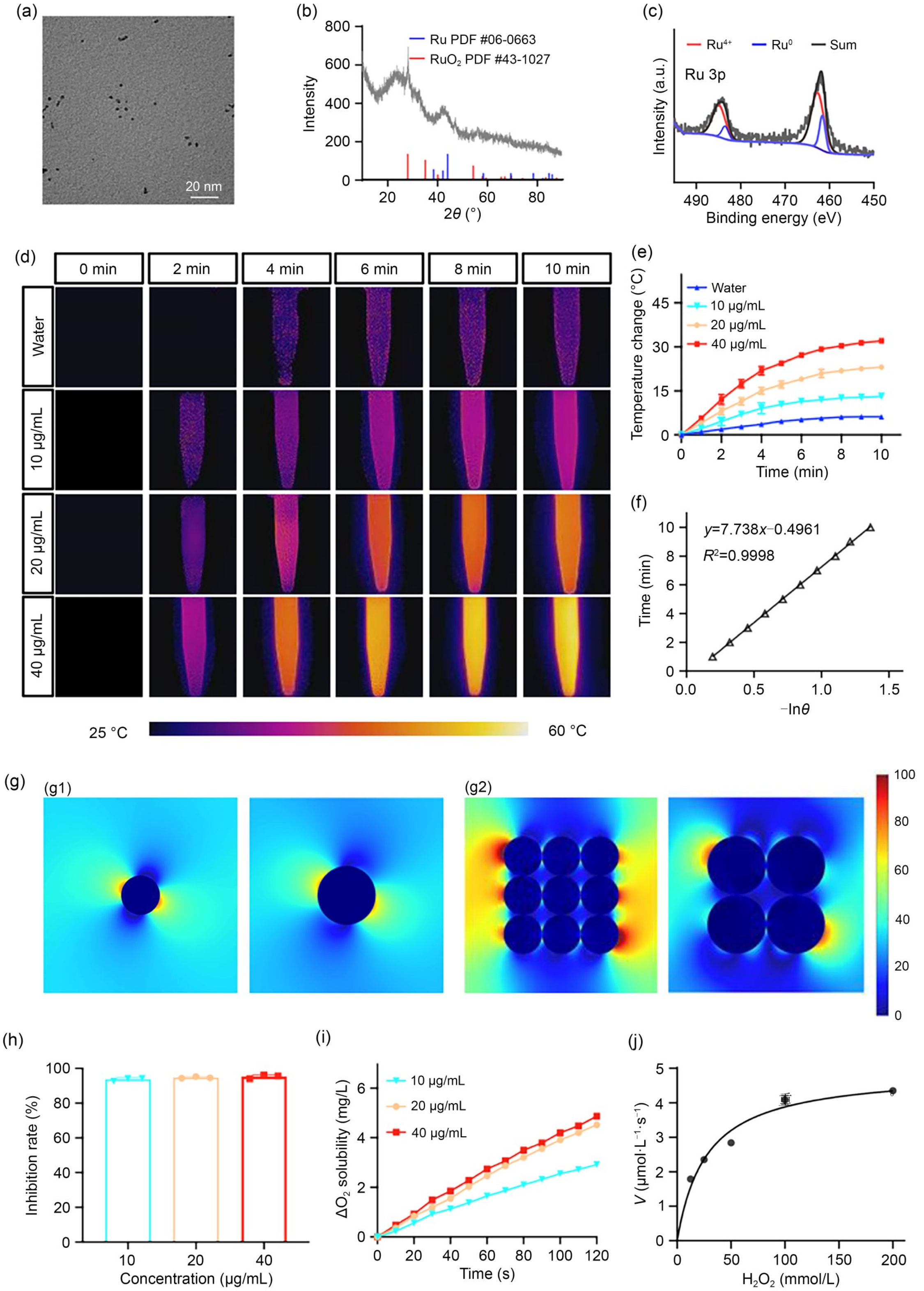

Fig. 1 Characterization of US-RuNPs. (a) TEM image of US-RuNPs. (b) XRD analysis of US-RuNPs. (c) Normalized Ru 3p XPS spectrum of US-RuNPs. Photothermal images (d) and temperature change curves (e) of different US-RuNPs concentrations under NIR laser irradiation at 2 W/cm^2. (f) PCE of US-RuNPs. (g) FDTD numerical simulations of RuNPs at the single-particle nanoscale (g1) and global effects from nanoparticles with the normalized projected area (g2). (h) SOD-like activity of US-RuNPs. (i) Oxygen generation ability of US-RuNPs in the presence of H_2O_2. (j) Michaelis–Menten fitting curve of the US-RuNPs. Data are shown as mean±standard deviation (*n*=3). TEM: transmission electron microscope; FDTD: finite-difference time-domain; PCE: photothermal conversion efficiency

properties of US-RuNPs, their surface was functionalized with methoxypolyethylene glycol thiol 2000 mPEG2k-SH to increase their water stability, resulting in the successful fabrication of monodisperse US-RuNPs with good colloidal stability (Fig. S1b in the supplementary information).

2.2 US-RuNPs exhibited outstanding photothermal properties

First, the photothermal performance of US-RuNPs was evaluated. The temperature of US-RuNPs displayed a concentration-dependent trend (Figs. 1d and 1e) as well as a power-dependent response under NIR laser irradiation (Fig. S2a in the supplementary information). Notably, the temperature of US-RuNPs (40 μg/mL) increased to 57 °C after 10 min NIR laser irradiation (2 W/cm^2). Moreover, US-RuNPs showed robust photothermal stability, maintaining maximum temperatures over six heating and cooling cycles under NIR laser irradiation (Fig. S2b in the supplementary information). The photothermal conversion efficiency (PCE, η) of US-RuNPs was determined to be 41.7%, corroborating their adept photothermal conversion capability (Fig. 1f). To explore the mechanism underlying the commendable photothermal properties of US-RuNPs, we synthesized larger-sized RuNPs with approximately 4 and 6 nm diameters (Fig. S3a in the supplementary information). As depicted in Fig. S3b (supplementary information), the smallest-sized RuNPs exhibited the greatest photothermal effect under NIR laser irradiation at the same concentration. Furthermore, finite-difference time-domain (FDTD) numerical simulations revealed that the smaller-sized RuNPs had an amplified electric field both at the single-particle nanoscale and the global effects from the nanoparticles with the normalized projected area (Fig. 1g).

2.3 US-RuNPs exhibited SOD-like and CAT-like activity

Next, we investigated the antioxidant activity of US-RuNPs. According to the SOD assay kit, 10 μg/mL of US-RuNPs could effectively catalyze superoxide anions ($\cdot O_2^-$) into oxygen and hydrogen peroxide (H_2O_2), demonstrating the robust SOD-like activity (Fig. 1h). The H_2O_2 decomposition capability of US-RuNPs was also evaluated. Both 20 and 40 μg/mL of US-RuNPs displayed admirable CAT-like activity, as evidenced by O_2 generation (Fig. 1i). The Michaelis constant (K_m) for US-RuNPs (27.16 mmol/L) was lower than that of the native CAT enzyme (57.67 mmol/L), suggesting 2.12-fold higher catalytic efficiency compared to that of the native enzyme (Fig. 1j). However, with increasing size, the catalytic efficiency of RuNPs decreased (Figs. S3c and S3d in the supplementary information).

Thus, it was certain that US-RuNPs possessed outstanding photothermal properties and antioxidant enzyme-like activity. Although they exhibited therapeutic potential, a more detailed evaluation of US-RuNPs in vitro and in vivo was required for the treatment of periodontitis.

2.4 US-RuNPs killed bacteria through PTT

F. nucleatum and *P. gingivalis* were selected as representative periodontitis-causing bacteria to evaluate the antibacterial quality of US-RuNPs. Under NIR laser irradiation, 40 μg/mL of US-RuNPs exhibited the best antibacterial effect, showing close to 0% bacterial survival (Figs. 2a and 2c). A weaker bactericidal ability was observed in the 20 μg/mL group. However, there were almost no antibacterial effects without NIR laser irradiation regardless of US-RuNPs concentration.

Subsequently, we investigated the capability of US-RuNPs to destroy or prevent biofilm formation. Similar to the previous tests, the effect was positively correlated with US-RuNPs concentration under NIR laser irradiation (Figs. 2b and 2d). For a US-RuNPs concentration of 40 μg/mL, there were only sporadic colonies.

Further, scanning electron microscopy (SEM) was used to observe changes in bacterial morphology under US-RuNPs treatment. As shown in Fig. 2e, the heat generated by US-RuNPs via PTT caused significant shrinkage of *F. nucleatum* and *P. gingivalis*.

2.5 US-RuNPs showed antioxidant effects in vitro

Human gingival fibroblasts (HGFs), typical periodontal-associated cells, were used to test the ability of US-RuNPs to combat oxidative stress. Figure 3a reveals increased HGFs proliferation under US-RuNPs treatment compared with the H_2O_2 group. Moreover, the cell viability in the 40 μg/mL group was close to that in the control group. 2',7'-Dichlorodihydrofluorescein diacetate (DCFH-DA) was employed to detect intracellular ROS. A higher US-RuNPs concentration yielded a greater antioxidant effect (Fig. 3b), and the fluorescent signal in the 40 μg/mL group was very weak, indicating the ability to eliminate ROS. The mitochondrial membrane potential (MMP) and apoptosis detection assay suggested that MMP changed due to H_2O_2 stimulation, leading to apoptosis. The capacity of US-RuNPs to resist oxidative stress strengthened with increasing concentrations, and the number of apoptotic cells decreased consequently (Fig. 3c).

Then, we investigated the impact of US-RuNPs on the proinflammatory responses of RAW 264.7 cells. As shown in Fig. 4a, lipopolysaccharide (LPS)-stimulated RAW 264.7 cells expressed higher inflammatory genes, including

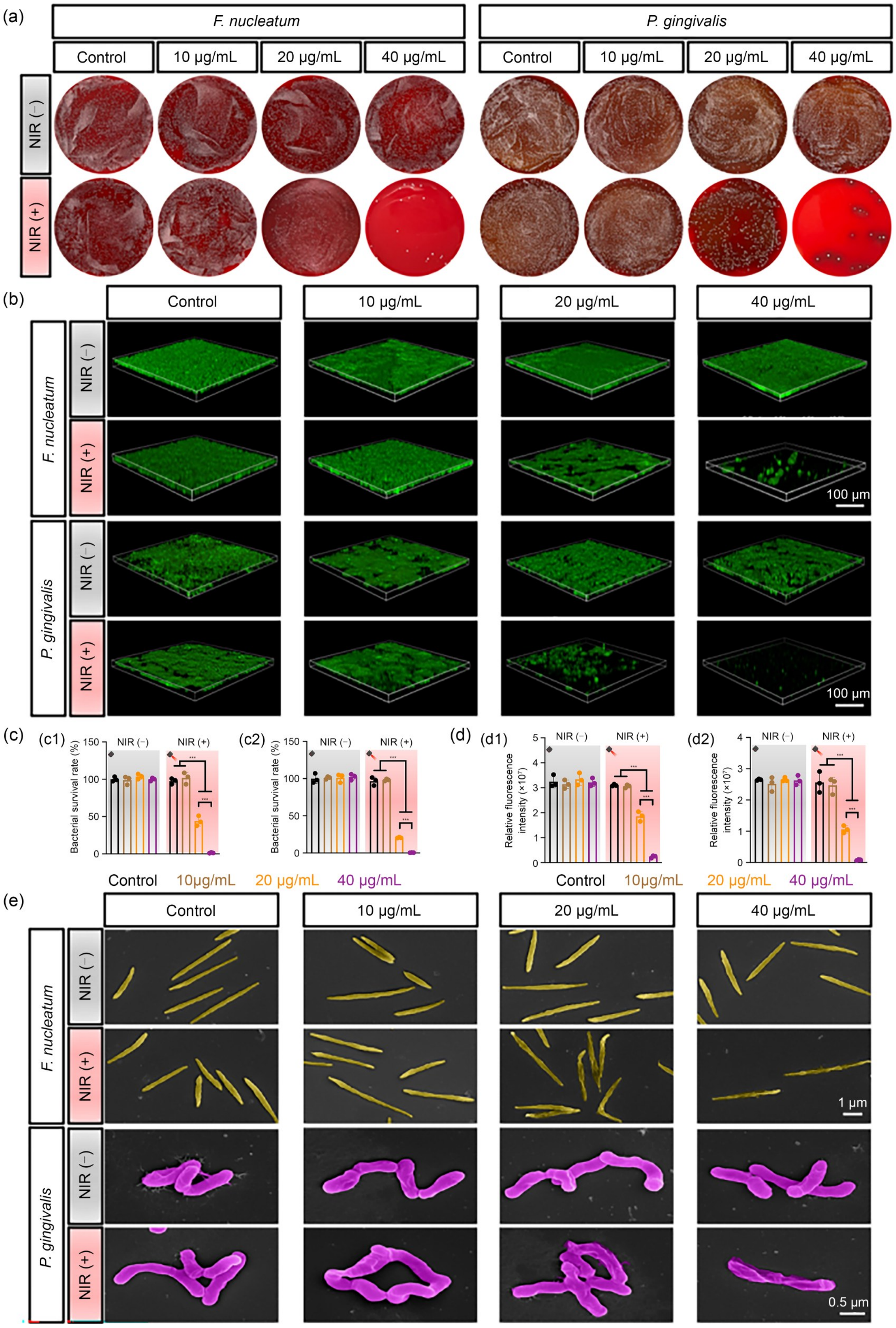

Fig. 2 Bacterial lysozyme-like effect of US-RuNPs. (a) Photos of bacterial colonies of *F. nucleatum* and *P. gingivalis* treated with different US-RuNPs concentrations with or without NIR laser irradiation. (b) 3D confocal images of *F. nucleatum* and *P. gingivalis* biofilms stained with SYTO 9 after different treatments. (c) Bacterial survival rate of *F. nucleatum* (c1) and *P. gingivalis* (c2) based on the number of bacterial colonies. (d) Relative fluorescence intensity of *F. nucleatum* (d1) and *P. gingivalis* (d2) biofilms. (e) SEM images of *F. nucleatum* and *P. gingivalis* under different treatments. Data are shown as mean±standard deviation (n=3). $^{***}P<0.001$

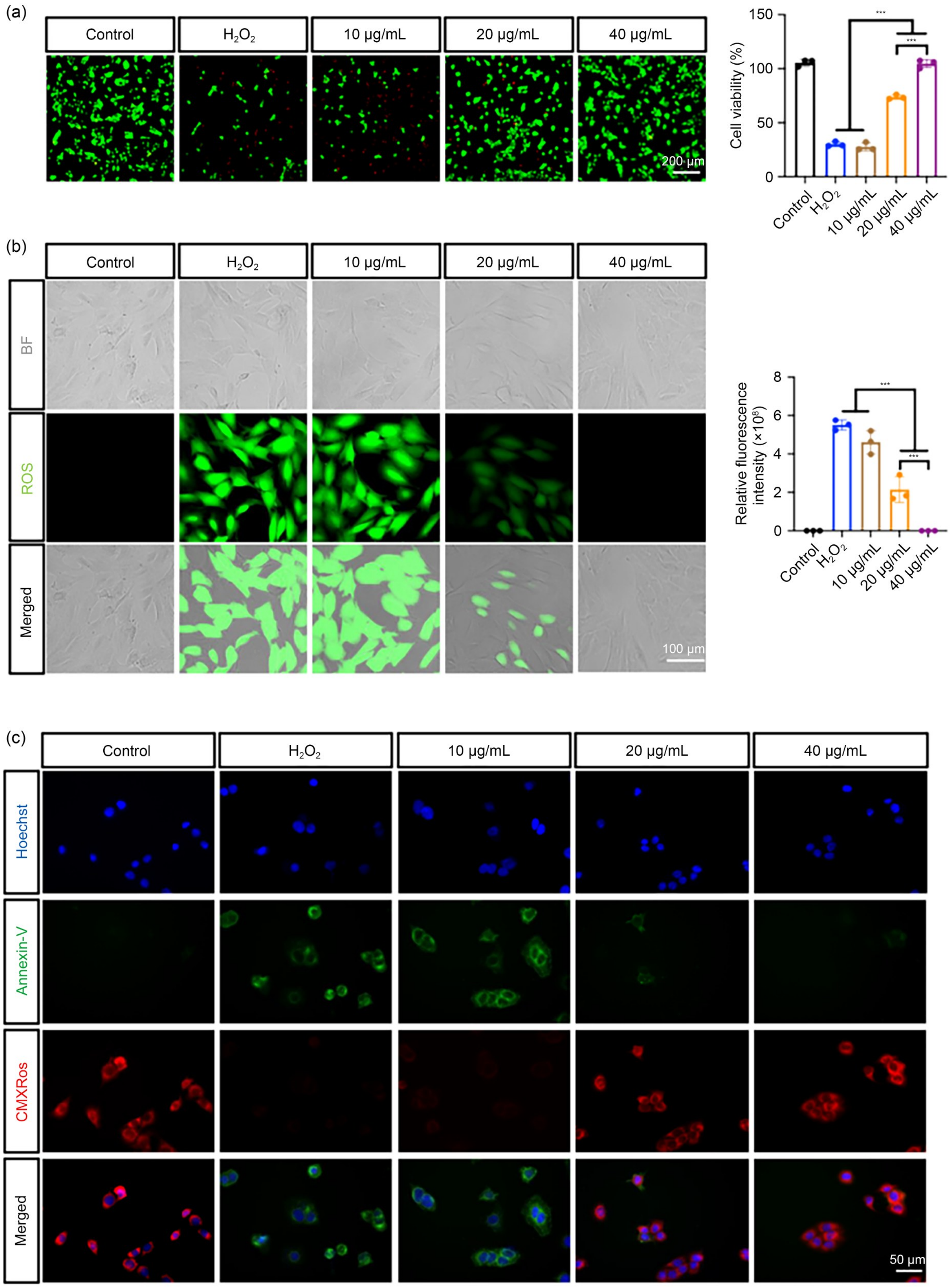

Fig. 3 Antioxidant activity of US-RuNPs in vitro. (a) Live/Dead staining and cell viability of HGFs after culturing with H_2O_2 or US-RuNPs+H_2O_2. (b) Fluorescence images and relative fluorescence intensity of intracellular ROS stained with DCFH-DA. (c) Images illustrating MMP changes and cell apoptosis of HGFs after cultured with H_2O_2 or US-RuNPs+H_2O_2. Living cells with MMP show red fluorescence while apoptotic cells show green fluorescence, and cell nuclei stained with Hoechst show blue fluorescence. Data are shown as mean±standard deviation (n=3). $^{***}P<0.001$. BF: bright field

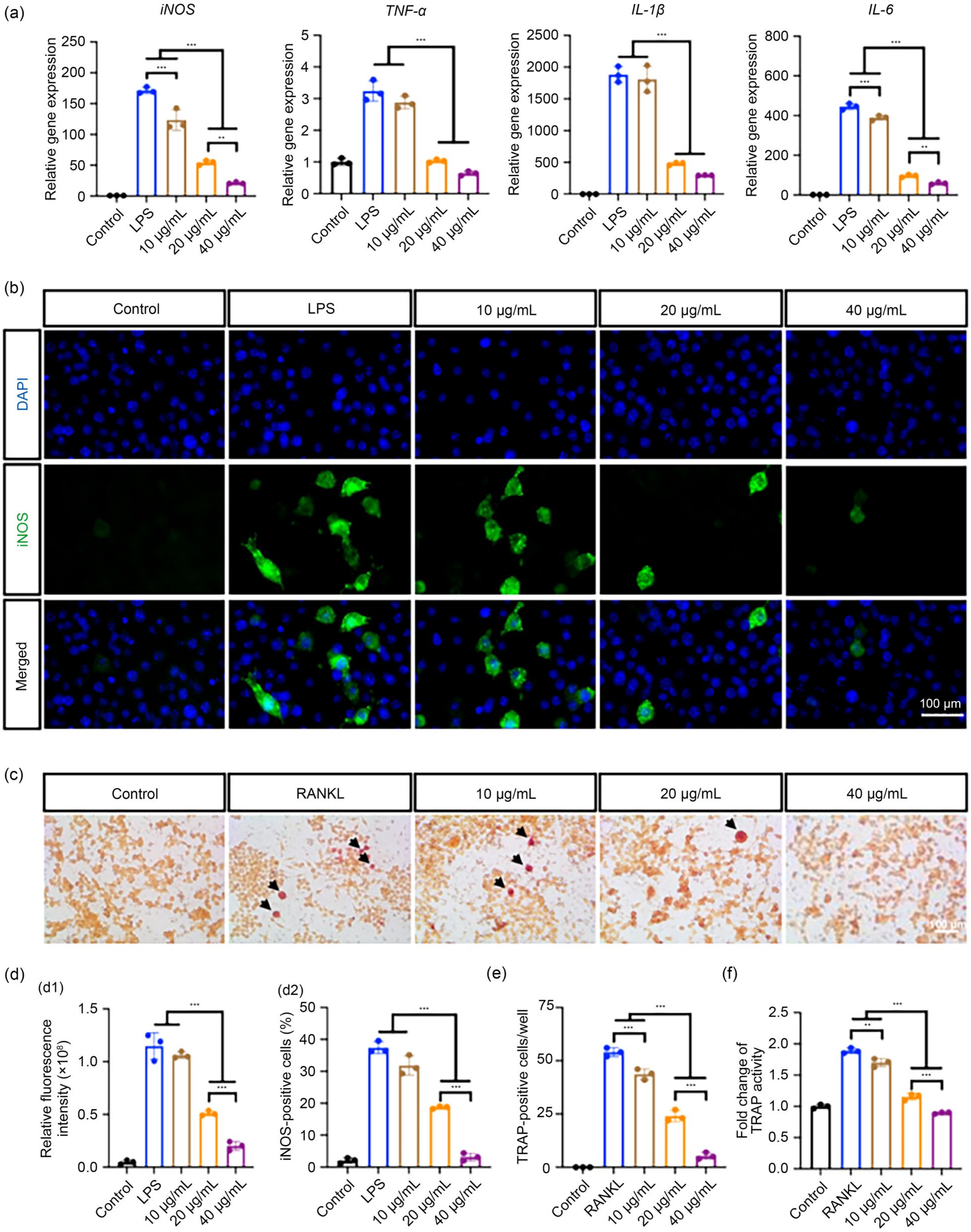

Fig. 4 Anti-inflammatory performance of US-RuNPs in vitro. (a) Relative gene expression of RAW 264.7 cells stimulated with 1 μg/mL LPS for 6 h and treated with different concentrations of US-RuNPs. Immunofluorescence images (b) and quantitative analysis (d) of iNOS protein expression in RAW 264.7 cells after different treatments. Images (c) and quantitative analysis (e) of TRAP-positive cells cultured with RANKL and different concentrations of US-RuNPs. Black arrows indicate TRAP-positive cells. (f) TRAP activity by TRAP assay kit of RAW 264.7 cells after different processes. Data are shown as mean±standard deviation (*n*=3). $^{**}P<0.01$, $^{***}P<0.001$. TRAP: tartrate-resistant acid phosphatase; RANKL: receptor activator of nuclear factor-kappa B ligand; DAPI: 4',6-diamidino-2-phenylindole

inducible nitric oxide synthase (*iNOS*), tumor necrosis factor-alpha (*TNF-α*), interleukin-1 beta (*IL-1β*), and interleukin-6 (*IL-6*), whereas treatment with 20 and 40 μg/mL of US-RuNPs significantly reduced their expression. Similarly, the immunofluorescence of the iNOS protein confirmed the anti-inflammatory properties of US-RuNPs (Figs. 4b and 4d). Finally, RAW 264.7 cells were stimulated with the receptor activator of nuclear factor-kappa B ligand (RANKL) to develop a model of osteoclast differentiation. The number of tartrate-resistant acid phosphatase (TRAP) positive cells and TRAP activity both decreased in a concentration-dependent manner (Figs. 4c, 4e, and 4f). The expression of RANKL-induced osteoclast-related genes, including *RANK*, *TRAP*, nuclear factor of activated T cells cytoplasmic 1 (*NFATc1*), and matrix metalloprotein-9 (*MMP9*), was similarly inhibited (Fig. S4 in the supplementary information).

2.6 US-RuNPs displayed satisfactory therapeutic efficacy for periodontitis in vivo

Given the promising in vitro performance of US-RuNPs, the therapeutic efficacy of US-RuNPs in vivo was investigated in rats suffering from periodontitis. According to previous studies, a rat model of periodontitis was achieved by ligature and *P. gingivalis* injection (Fig. 5a). Then, rats were randomly divided into four groups to receive different concentrations of US-RuNPs, followed by NIR laser irradiation every 3 d, as the US-RuNPs were nearly cleared from periodontal pockets within 72 h (Fig. S5 in the supplementary information). As shown in Fig. 5b, 40 μg/mL of US-RuNPs elevated the temperature to approach 55 °C within 10 min while the phosphate-buffered saline (PBS) control produced no obvious changes. Considering the influence of hyperthermia on normal tissues, we detected Caspase-1 expression by immunohistochemical (IHC) staining. As shown in Fig. S6 (supplementary information), there was no significant difference among groups, indicating that the heat produced through PTT would not cause damage to normal tissues.

After treatment, the gingival crevicular fluid was collected to assess the bacterial burden. The number of bacterial colonies decreased in the 40 μg/mL group, indicating good antibacterial performance (Fig. 5c). Based on the micro-computed tomography (micro-CT) data, bone loss was suppressed by US-RuNPs (Fig. 5d). The ratio of alveolar bone loss to root length (ABL/RL) reached 70.70% in the PBS group (Fig. 5e), but declined to almost normal levels (20.15%) in the 40 μg/mL group. Meanwhile, the analysis of other bone parameters revealed greater bone volume per tissue volume (BV/TV) and trabecular thickness (Tb.Th), as well as smaller trabecular separation (Tb.Sp) under treatment with US-RuNPs. Hematoxylin and eosin (H&E) staining showed the presence of remarkable immune cells in the PBS group (Figs. 6a and 6d). The result was consistent with IHC staining, which displayed higher IL-6 expression in periodontitis rats without US-RuNPs treatment (Figs. 6c and 6f). In contrast, 40 μg/mL of US-RuNPs could decrease inflammatory infiltration. What's more, soft tissue regeneration was evidenced by Masson staining (Figs. 6b and 6e), and the collagen volume fraction increased from 16.88% to 57.64%.

2.7 US-RuNPs showed good biocompatibility

The live/dead staining and cell counting kit-8 (CCK-8) assay indicated good biocompatibility at different US-RuNPs concentrations without NIR laser irradiation. Although the cell viability of HGFs decreased after 1 d in the 20 and 40 μg/mL groups under NIR laser irradiation, the cells could gradually proliferate and recover. On the 3rd day, there was no significant difference between the 20 μg/mL and control groups, while the cell viability in the 40 μg/mL group recovered to 78.86% (Fig. 7a).

We also confirmed the biosafety of US-RuNPs in vivo through H&E staining of vital organs, revealing no abnormal morphological or histological changes among groups (Fig. 7b).

3 Discussion

As one of the most prevalent diseases in the world, periodontitis is triggered by the colonization of bacteria. The gradual destruction of periodontal supporting tissues is caused by the imbalance between the endogenous enzyme system and the panic host inflammatory response [46]. Traditional clinical therapy is not ideal due to its poor efficiency in bacterial elimination and immunoregulation. With the rise of nanotechnology, metal-based nanozymes have received the lion's share of attention in periodontitis therapy. However, nanozymes that integrate both antibacterial properties and antioxidant ability, which are key in periodontitis therapy, have rarely been reported. Taking convenient manufacturing, simple composition, and obvious effects as the principle, we introduced US-RuNPs as nanozymes with excellent bactericidal performance under NIR and ROS-scavenging ability for periodontitis therapy in this study (Fig. 8).

PTT is increasingly used for biological applications due to its advantages compared to traditional antibiotics. As an essential factor for PTT, PTAs should possess high PCE [39]. It was reported that the PCE of Fe_3O_4 nanoparticles, Pt nanoparticles, and WO_{3-x} was around 25% [47]. The PCE of the Ru-SiO_2@polydopamine nanoplatform (synthesized by Deng et al.) and PdRu-RCE@PCM nanoparticles (synthesized by Cen et al.) were about 36% [48, 49]. In contrast, US-RuNPs used in our study exhibited a PCE of 41.7% (Fig. 1f). We attributed the commendable photothermal

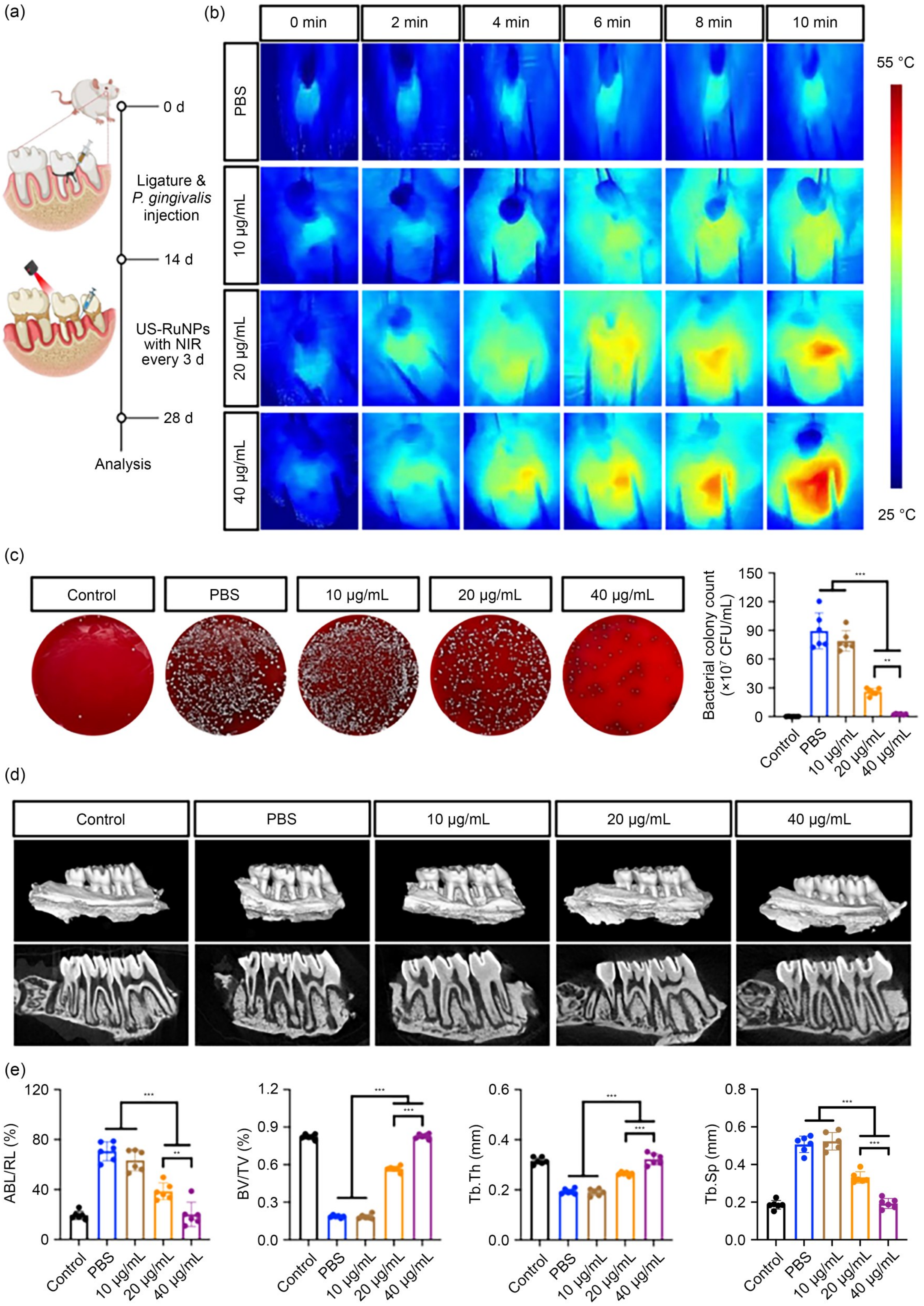

Fig. 5 Therapeutic effect of US-RuNPs against periodontitis in vivo. (a) Schematic illustration of the establishment and treatment of periodontitis in rats. (b) Digital photos of temperature changes in periodontal tissues treated with different concentrations of US-RuNPs under NIR laser irradiation. (c) Photos and quantitative analysis of bacterial colonies in periodontal pockets after different treatments. (d) 3D micro-CT-reconstructed and bucco-palatal section images of the maxillary molars. (e) Quantitative analysis of bone parameters after different treatments. Data are shown as mean±standard deviation (n=6). $^{**}P<0.01$, $^{***}P<0.001$

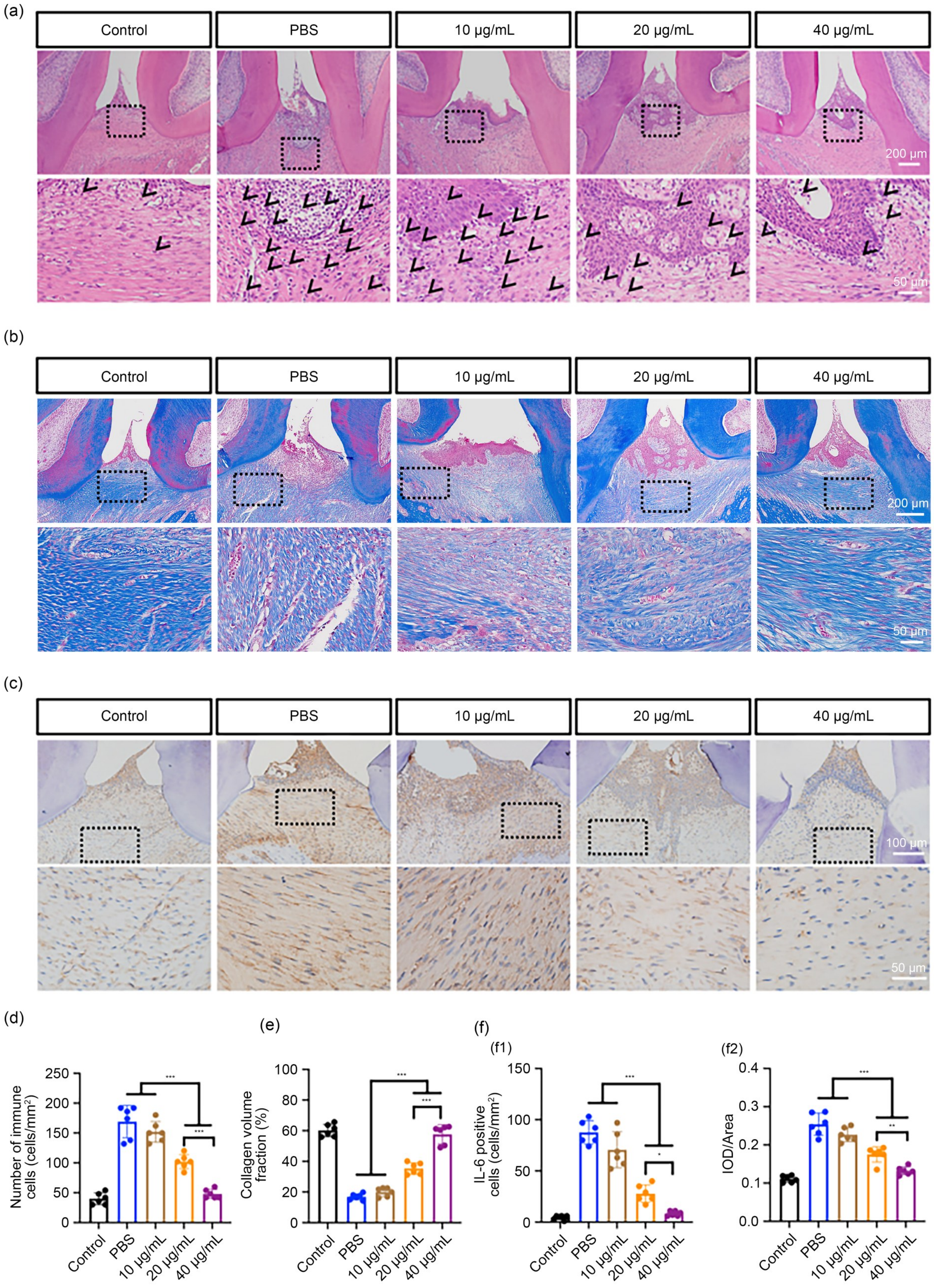

Fig. 6 Histological evaluation of periodontal tissues. (a) H&E staining (black arrows indicate immune cells). (b) Masson's trichrome staining. (c) IHC staining of IL-6. (d–f) Quantitative analysis of histological features. Data are shown as mean±standard deviation (n=6). $^{*}P<0.05$, $^{**}P<0.01$, $^{***}P<0.001$. IOD: integrated optical density

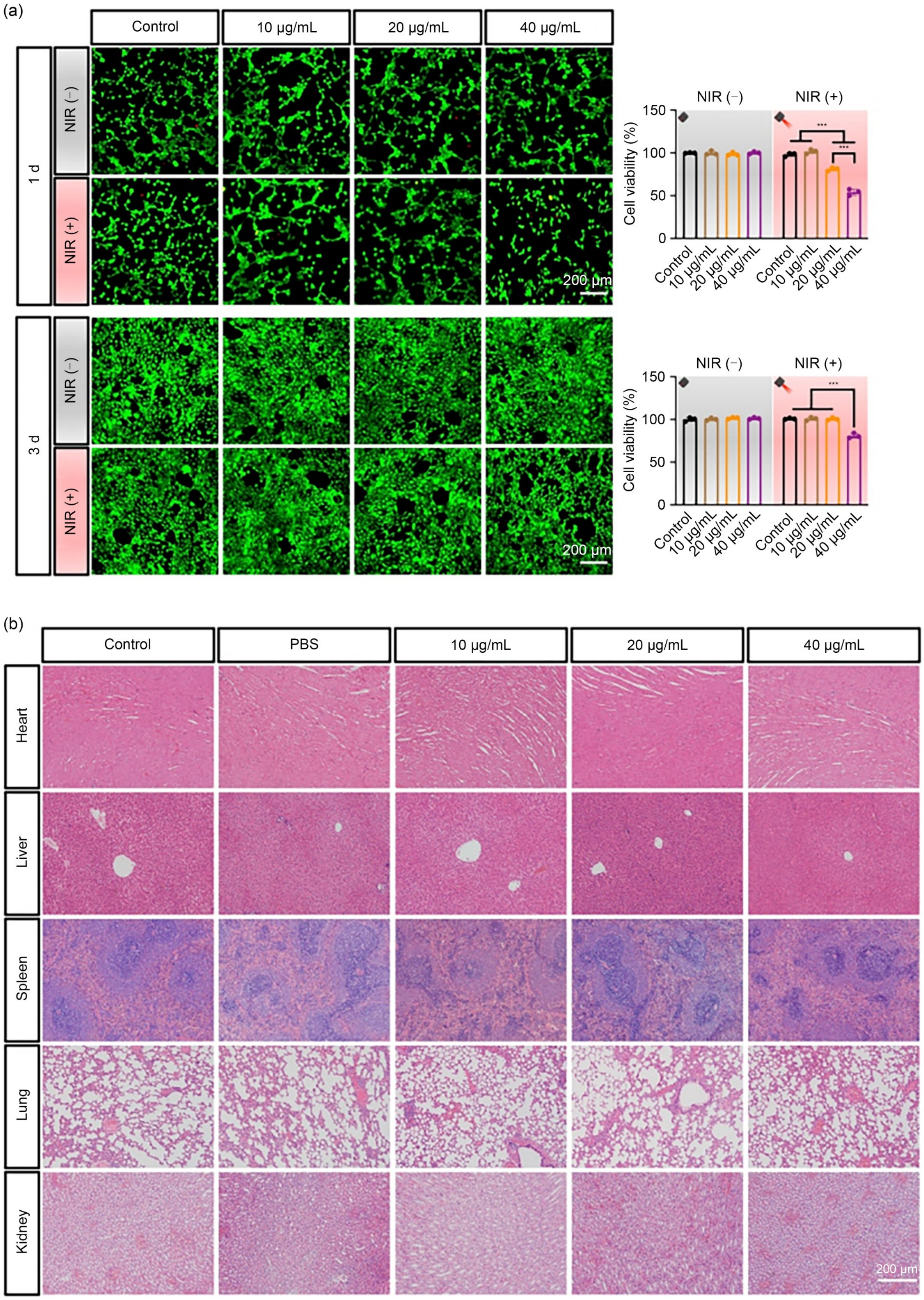

Fig. 7 Biocompatibility of US-RuNPs. (a) Live/Dead staining and cell viability of HGFs after being treated with different concentrations of US-RuNPs with or without NIR laser irradiation. (b) H&E staining of vital organs in rats receiving different treatments. Data are shown as mean±standard deviation (n=3). $^{***}P$<0.001

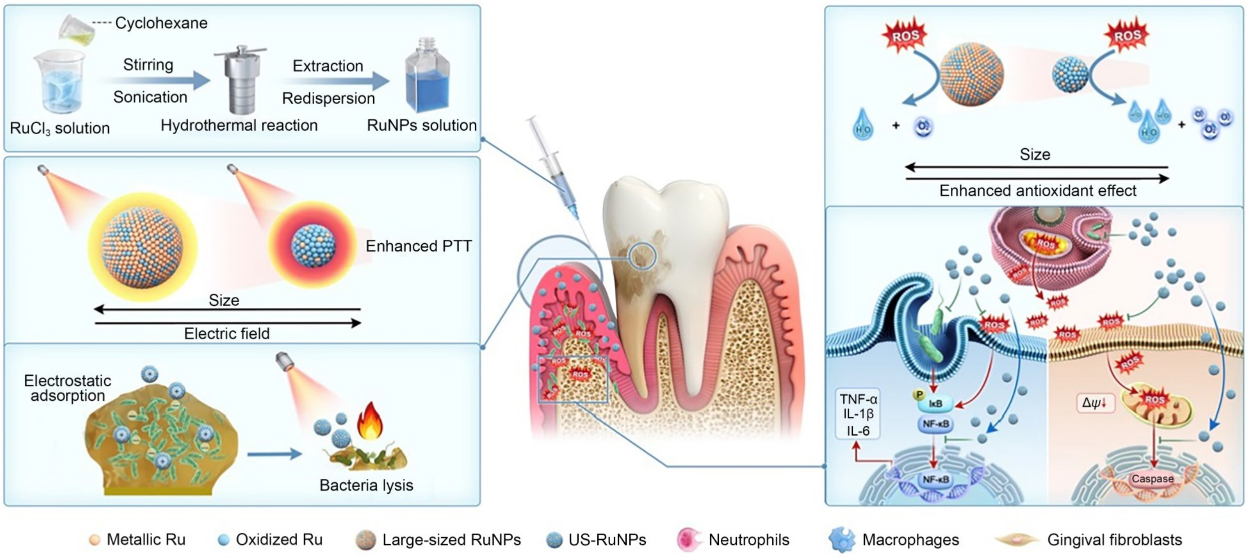

Fig. 8 Schematic illustration of US-RuNPs in the principle of therapeutic mechanisms. US-RuNPs were synthesized using an emulsion-based solvothermal method. Compared to large-sized RuNPs, US-RuNPs enhanced light coupling and produced a stronger electric field, exhibiting bacterial lysozyme-like activity. Furthermore, US-RuNPs with a higher surface area and a higher proportion of oxidized Ru exhibited better antioxidant enzyme-like effects. Moreover, US-RuNPs could be delivered into the deep sites of the periodontal tissues. Thus, US-RuNPs efficiently removed bacteria and scavenged ROS in vivo, promoting the regeneration of periodontal tissues

properties of US-RuNPs to their ultrasmall size. Metal nanoparticles generate heat when electromagnetic light waves resonate with the oscillation of surface electrons. In principle, improved PCE can be achieved by enhancing light coupling [50]. According to the Mie theory, both light absorption and scattering increase with the increase of nanoparticle size, as does the scattering-to-absorption ratio, which implies that light absorption is more determinant for smaller-sized nanoparticles [51]. Jauffred et al. considered that smaller-sized nanoparticles were more efficient absorbers when the absorption efficiency (Q_{abs}) was defined as the absorption cross section (C_{abs}) normalized by the projected area [52]. Subsequently, the absorbed light induced both the excitation of free electrons and the generation of electric fields on the surface of the nanoparticles [53]. Our previous study revealed that the electric fields of nanoparticles were positively correlated with the localized surface plasmon resonance and the photothermal effect [54]. Thereby, smaller-sized RuNPs could enhance the coupling of light and produce stronger electric fields, improving the photothermal effect. Consistent with our hypothesis, US-RuNPs had amplified electric fields both on the nanoparticle surfaces and in the nanoparticle spaces, significantly boosting the photothermal performance (Fig. 1g; Fig. S3b in the supplementary information). Furthermore, US-RuNPs had a high presence of oxidized Ru on the surface (Fig. 1c). The high positive charge density allowed US-RuNPs to selectively interact with the negatively charged surface of the bacteria. Under NIR laser irradiation, US-RuNPs could quickly remove bacteria (Figs. 2a–2d) by disrupting cell wall integrity (Fig. 2e). The bactericidal mechanism was a highly selective and efficient cell lytic process, analogous to that of phage lysozyme [55, 56].

US-RuNPs also exhibited superior antioxidant enzyme-like activity (Figs. 1h–1j). Decreasing the size of RuNPs could increase SOD-like and CAT-like activities. Researchers discovered that $\cdot O_2^-$ and the hydroperoxyl radicals ($\cdot$OOH) could be easily adsorbed on the metal surface [57]. Thus, US-RuNPs with higher specific surface area could expose more active sites for substrates and display better SOD-like activity (Fig. S3c in the supplementary information) [58]. Moreover, a higher specific surface provided smaller-sized RuNPs with a higher proportion of oxidized Ru on the surface. The free energy barrier to decompose H_2O_2 was lower in oxidized Ru than in metallic Ru [59]. As a result, US-RuNPs had better CAT-like activity (Fig. S3d in the supplementary information). Because of their extraordinary antioxidant enzyme-like activity, US-RuNPs could protect HGFs under oxidative stress (Fig. 3a) and inhibit the inflammatory responses of RAW 264.7 cells (Fig. 4a).

Finally, US-RuNPs displayed significant efficacy in periodontitis therapy in vivo. Modern studies have demonstrated that ROS generated by the host immune system in response to bacterial pathogen stimulation establish an oxidative-stressed environment that underlay the pathogenesis of periodontitis [60, 61]. Above all, US-RuNPs under NIR exhibited bacterial lysozyme-like activity to fight against pathogens. In the clinic, deep periodontal pockets limit the efficiency of mechanical therapies. Moreover, some bacteria invade the gingival epithelium and dentinal tubules, impeding the permeation of antibiotics [62, 63]. However, US-RuNPs, around 2 nm, could be easily delivered into deep sites and traverse the tight connections of the epithelia [64]. Moreover, NIR light can penetrate deeper tissues than visible light because it experiences less scattering in biological tissues [65, 66]. Although hyperthermia had a slight impact on normal cells when killing bacteria, Kang et al. considered that the temporary effect of PTT was acceptable because the duration of hyperthermia was very short and tissues had strong self-healing ability [67]. As our results indicated, US-RuNPs under NIR quickly reached high temperatures and killed bacteria in a short time, reducing the possibility of side effects induced by hyperthermia on normal tissues (Figs. 5b and 5c; Fig. S6 in the supplementary information). Furthermore, US-RuNPs without NIR still could balance the microenvironment for inflammation resolution by scavenging ROS. Their small size endowed US-RuNPs with excellent SOD-like and CAT-like activity even at the lower concentration, which indicated that they had a relatively long-term effect in the salivary environment. Hence, US-RuNPs not only reduced infiltration of immune cells in soft tissues (Figs. 6a–6d), but also significantly promoted the regeneration of periodontal hard tissues (Figs. 5d and 5e). Moreover, nanoparticle elimination has important impacts on biosafety. Generally, small-sized nanoparticles are more easily cleared by the kidneys [64]. The biosafety of US-RuNPs in vivo was also proved in our study (Fig. 7b).

Nevertheless, there are some limitations in our study. First, the dental plaque in periodontitis is clinically more complex than the biofilms used in the experiment. It is better to evaluate the antiplaque effect of US-RuNPs on the dentin surface. Second, as periodontitis is linked with systemic health, it is meaningful to explore whether US-RuNPs can exert therapeutic effects on periodontitis accompanied by systemic disease. Finally, although our study proposes a more efficient treatment strategy, further research is needed to understand the underlying mechanism.

4 Conclusions

In this work, we synthesized US-RuNPs with a diameter of approximately 2 nm. The small size endowed US-RuNPs with special advantages in terms of their photothermal properties and ROS-scavenging ability. As a result, NIR-responsive US-RuNPs showed bacterial lysozyme-like activity to fight against periodontitis pathogens even in deep sites. Moreover, US-RuNPs without NIR could exhibit antioxidant enzyme-like activity continuously, ensuring subsequent periodontal tissue regeneration. Therefore, our study provides a minimally invasive, effective, and precise treatment strategy for periodontitis. We also believe that US-RuNPs hold promise for the treatment of other diseases with bacterial infection and unbalanced ROS metabolism.

5 Materials and methods

5.1 Synthesis and characterization of RuNPs

RuNPs were synthesized using the emulsion-based solvothermal method. For US-RuNPs, ruthenium chloride hydrate (50 mg; Aladdin, China) was dissolved in distilled water (13 mL). Then, oleylamine (0.2 g) was dissolved in cyclohexane (2 mL; Aladdin) and added to the ruthenium chloride solution. After sonicating for 10 min and stirring for 1 h, the mixture was transferred into a Teflon-lined autoclave (20 mL) and maintained at 160 °C for 12 h. After cooling to room temperature, cyclohexane (5 mL) was added to extract the US-RuNPs. After adding ethanol (15 mL; Sinopharm, China) to the extract liquor, the mixture was centrifuged for 10 min, and the precipitate was further washed in ethanol three times and redispersed in chloroform (Sinopharm) for further use. For the large-sized RuNPs, 0.4 and 0.8 g of oleylamine were added to the reaction system to synthesize RuNPs with a diameter of approximately 4 and 6 nm, respectively. The Ru concentration was measured by inductively coupled plasma mass spectrometry (ICP-MS) (PerkinElmer NexION 300X, USA). Transmission electron microscopy (TEM) images were obtained using a Hitachi HT770 microscope (Hitachi High-Tech, Japan). XRD patterns were acquired with a PANalytical X’Pert PRO diffractometer (Malvern Panalytical, the Netherlands), while XPS was conducted on a Thermo Scientific ESCALAB 250 Xi XPS system.

5.2 Surface modification of RuNPs

mPEG2k-SH (10 mg) and RuNPs (1 mg) were mixed in chloroform (5 mL). After sonication for 1 h, the mixture was dried under rotary evaporation for 1 h. Then, distilled water (1 mL) was added to re-disperse the RuNPs. The excessive mPEG2k-SH was removed by ultrafiltration. The hydrodynamic size was measured by dynamic light scattering (DLS) using a Zetasizer Nano ZS90 (ZEN 3690, Malvern Instruments, UK).

5.3 Photothermal properties of RuNPs

To investigate their photothermal capacity, RuNPs in deionized water were transferred to 1.5-mL centrifuge tubes and irradiated under an 808-nm NIR laser. The temperature was measured every minute using a temperature controller (AI-518P, Yudian Automation Technology, China). The temperature changes were also recorded every 2 min using an infrared thermographic camera (H21Pro, HIKMICRO, China). To study the photothermal stability of the RuNPs, 40 μg/mL of RuNPs were exposed to an NIR laser at the power density of 2 W/cm^2 for 10 min and cooled to room temperature. Then, the temperature was monitored for six on-off laser cycles. The following equations calculate the photothermal conversion efficacy (η):

$$\eta = \frac{hS\left(T_{\text{Max}} - T_{\text{Surr}}\right) - Q_{\text{Dis}}}{I\left(1 - 10^{-A_{808}}\right)},$$

$$\theta = \frac{T - T_{\text{Surr}}}{T_{\text{Max}} - T_{\text{Surr}}},$$

$$t = -\tau_{\text{s}} \ln \theta,$$

$$\tau_{\text{s}} = \frac{mC}{hS},$$

$$Q_{\text{Dis}} = hS\left(T_{\text{Max,PBS}} - T_{\text{Surr}}\right).$$

Here, h is the heat transfer coefficient of the container, S is the surface area of the container, T_{Max} is the maximum temperature of the solution, T_{Surr} is the room temperature, Q_{Dis} represents the energy input of the background, I is the laser power, A_{808} is the absorbance value of the RuNPs at 808 nm, C and m indicate the heat capacity and mass of the solvent respectively, θ is introduced to obtain hS, T indicates the temperature at the corresponding time, τ_{s} is the time constant of the sample system, and $T_{\text{Max,PBS}}$ is the maximum temperature of PBS.

The FDTD solution software package (MEEP) was used to numerically calculate the near-field electromagnetic field distributions of the RuNPs.

5.4 SOD-like activity of RuNPs

The SOD-like activity of RuNPs at different concentrations (10, 20, and 40 μg/mL) was measured using a Superoxide Dismutase (SOD) Assay Kit-WST (Dojindo, Japan) following the manufacturer's protocol.

5.5 CAT-like activity of RuNPs

Different volumes (0.05, 0.10, and 0.20 mL) of 1 mg/mL RuNPs and 0.05 mL of 100 mmol/L H_2O_2 (Sinopharm Chemical Reagent Co., China) were added to deionized water to a final volume of 5 mL. The final concentrations were 1 mmol/L H_2O_2 and 10, 20, or 40 μg/mL RuNPs in the system. The generated oxygen concentration was evaluated using an oxygen electrode with a Dissolved Oxygen Meter JPB-607 (INESA Scientific Instrument Co., China) at room temperature.

The CAT-like activity of RuNPs was measured kinetically at different H_2O_2 concentrations (12.5, 25, 50, 100, and 200 mmol/L) with a fixed Ru concentration of 5 μg/mL in 5 mL deionized water. Briefly, the time-dependent change in dissolved oxygen concentration after H_2O_2 addition was recorded, and the initial velocities (v_0) were calculated from the linear range of the first 30 s. The v_0 values were plotted against H_2O_2 concentrations, and the Michaelis–Menten curve was fitted using GraphPad Prism 8.0.2.

5.6 Antibacterial test

F. nucleatum (ATCC 25586) and *P. gingivalis* (ATCC 33277) were used to evaluate the antimicrobial activity of US-RuNPs. Bacteria were cultured in fastidious anaerobe broth (FAB; Solarbio, China) in an anaerobic incubator at 37 °C.

A total of 100 μL of the bacterial suspension at a density of 10^6 CFU/mL (CFU: colony-forming unit) was seeded in a 96-well plate. Different US-RuNPs concentrations (10, 20, or 40 μg/mL) were added into FAB with or without NIR laser irradiation (2 W/cm^2, 10 min). Bacteria cultured without US-RuNPs were used as the control group. After 48 h, 20 μL of diluted bacterial suspension was spread onto Columbia blood agar (BKMAM, China). Then, the agar plates were anaerobically incubated at 37 °C for 96 h, and a camera was used to record the CFU. The bacterial survival rate (r_{bs}) was calculated using the following formula:

$$r_{\text{bs}} = \frac{\text{CFUs}_{\text{Experiment}}}{\text{CFUs}_{\text{Control}}} \times 100\%,$$

where $\text{CFUs}_{\text{Control}}$ represents the average number of bacterial colonies in the control group and $\text{CFUs}_{\text{Experiment}}$ represents the number of bacterial colonies in the experimental groups.

To investigate the anti-biofilm effect of US-RuNPs, sterilized cell climbing sheets were placed in a 24-well plate. A 500-μL bacterial suspension at a density of 10^7 CFU/mL was seeded onto the sheets. Bacterial groups were the same as above. After 72 h, the sheets were washed three times with PBS (Servicebio, China). Then, the biofilms were stained with SYTO 9 (Invitrogen, USA) according to the manufacturer's instructions and observed using a laser confocal microscope (Leica, Germany).

In a separate experiment, the sheets were rinsed three times with PBS after 48 h of culture. The bacteria on the sheets were fixed with 2.5% glutaraldehyde solution (Sinopharm, China) at 4 °C overnight, followed by dehydration with a graded ethanol series (30%, 50%, 70%, 90%, and 100%). After drying, samples were treated with gold sputtering for SEM (Nova Nano 450, Czech) observation.

5.7 Cell culture

HGFs (Pricella, China) and RAW 264.7 cells (Oricell, China) were chosen for in vitro experiments. Cells were cultured in media consisting of Dulbecco's modified Eagle medium (DMEM; Cienry, China), 10% fetal bovine serum (FBS; Gibco, USA), and 1% penicillin-streptomycin (Vivacell, China) with 5% CO_2 at 37 °C. The media were changed every 2 d.

5.8 Biocompatibility assay in vitro

A total of 100 µL of HGFs suspension was seeded in a 96-well plate at a density of 2.5×10^3 cells/well. After 24 h, the cells were treated with different concentrations of US-RuNPs (10, 20, and 40 µg/mL). Cells cultured without US-RuNPs were set up as the control group. In the NIR groups, the cells were exposed to NIR laser irradiation at 2 W/cm^2 for 10 min. After 24 and 72 h, we replaced the supernatant with 100 µL of fresh media and 10 µL of CCK-8 solution (Glpbio, China) and incubated cells at 37 °C for 2 h. The absorbance at 450 nm was measured using a microplate reader (Molecular Devices, USA), and the cell viability was calculated using the following formula:

$$\text{Cell Viability}=\text{OD}_{\text{Experiment}}/\text{OD}_{\text{Control}}\times100\%, \qquad (1)$$

where $\text{OD}_{\text{Experiment}}$ and $\text{OD}_{\text{Control}}$ represent the optical densities of the experimental and control groups, respectively.

In a separate experiment, we replaced the supernatant with 4 µmol/L Calcein acetoxymethyl ester (Calcein AM) and 4.5 µmol/L propidium iodide (PI) (MKBio, China) and incubated cells at 37 °C for 15 min. Then, cells were observed using an inverted fluorescence microscope (EVOS M5000, Invitrogen) for live/dead staining.

5.9 In vitro antioxidant efficacy of US-RuNPs

A total of 100 µL of HGFs suspension was seeded into a 96-well plate at the density of 2.5×10^3 cells/well. After 24 h, cells were cocultured with 500 µmol/L H_2O_2 and different US-RuNPs concentrations (10, 20, and 40 µg/mL) for another 24 h. Cells cultured in the medium without treatment were used as the control group. Cell viability was evaluated by the CCK-8 assay and calculated using Eq. (1).

In a separate experiment, cells were treated with 4 µmol/L Calcein-AM and 4.5 µmol/L PI, incubated at 37 °C for 15 min, and observed using an inverted fluorescence microscope for live/dead staining.

The Reactive Oxygen Species Assay Kit (Beyotime, China) was used to detect the intracellular ROS level. To that end, 500 µL of HGFs suspension was seeded in a 24-well plate at a density of 1×10^4 cells/well. Cell treatment was the same as above. Then, cells were washed with PBS three times and incubated with 10 µmol/L DCFH-DA at 37 °C for 20 min. The intracellular ROS level was observed using an inverted fluorescence microscope.

To investigate cell apoptosis caused by ROS, a mitochondrial membrane potential and apoptosis detection kit (Beyotime) was used. As above, cells were washed with PBS three times after being cultured with H_2O_2 or US-RuNPs+H_2O_2 for 24 h. Then, cells were stained with Annexin V-FITC, Mito-Tracker Red CMXRos, and Hoechst according to the manufacturer's instructions and observed using an inverted fluorescence microscope.

5.10 In vitro anti-inflammatory evaluation of US-RuNPs

For this, 500 µL of the RAW 264.7 cell suspension was seeded in a 24-well plate at a density of 3×10^4 cells/well. After 24 h, LPS (Sigma-Aldrich, USA) was added to the media at 1 µg/mL for another 6 h. Then, the supernatant was replaced by media containing different concentrations of US-RuNPs (10, 20, and 40 µg/mL). Cells cultured in media without treatment were set up as the control group. After 24 h, cells were collected using TRIzol (Thermo, USA). The expression of pro-inflammatory related genes, including *iNOS*, *TNF-α*, *IL-1β*, and *IL-6*, was evaluated by a real-time fluorescence quantitative polymerase chain reaction (qPCR) assay. The primer sequences used in qPCR were described in Table S2 (supplementary information).

In a separate experiment, cells were washed with PBS three times, fixed with 4% paraformaldehyde (Solarbio) for 20 min, and permeabilized with 1% Triton X-100 for 10 min. After blocking with 2% bovine serum albumin (BSA; Solarbio) and 2% FBS for 1 h, cells were incubated with iNOS antibody (1∶400; Cell Signaling, #13120, USA) at 4 °C overnight. Then, cells were washed with 0.05% Tween-20 (VETEC, USA) and incubated with iFluor 488 Conjugated Goat anti-rabbit IgG Polyclonal Antibody (1∶500; HUABIO, China) at room temperature for 2 h. Then, cells were washed again with 0.05% Tween-20 and stained with 4',6-diamidino-2-phenylindole (DAPI; Applygen, China). iNOS-positive cells were observed using an inverted fluorescence microscope.

5.11 In vitro effect of US-RuNPs on osteoclast differentiation

A total of 500 µL of the RAW 264.7 cell suspension was seeded in a 24-well plate at a density of 1×10^4 cells/well. After 24 h, cells were treated with 50 ng/mL RANKL (MCE, USA) and different concentrations of US-RuNPs (10, 20, and 40 µg/mL) for 7 d. Cells cultured in media without treatment were used as the control group. TRAP-positive cells were stained by a TRAP staining kit (Servicebio, China) and observed with an inverted microscope (Olympus, Japan). To further investigate the effect of US-RuNPs on osteoclast differentiation, cells were lysed with a radio immunoprecipitation assay (RIPA) lysis buffer (Applygen) after culture and the TRAP activity of the cells was quantified using a TRAP assay kit (Beyotime). In addition, the expression of osteoclast-related genes, including *RANK*, *TRAP*, *NFATc1*, and *MMP9*, was evaluated by qPCR. The primer sequences used in qPCR were described in Table S2.

5.12 Animal experiment

Six-week-old female Sprague–Dawley rats (Slaccas, China) were chosen to test the therapeutic effect of US-RuNPs in vivo. Rats were anesthetized with 1% pentobarbital sodium (Sigma-Aldrich) by intraperitoneal injection. Then, a nylon thread with a diameter of 0.2 mm (Chenghe, China) was ligatured around the maxillary second molar. Meanwhile, 100 μL of *P. gingivalis* suspension was injected around the maxillary second molar every 2 d. After two weeks, we removed the threads and checked the periodontitis models. Then, rats were treated with 100 μL of PBS or different concentrations of US-RuNPs solution (10, 20, and 40 μg/mL) accompanied by NIR laser (2 W/cm^2, 10 min) irradiation every 3 d for another 14 d. Normal rats were used as a control group. Temperature changes in periodontal tissues were recorded every 2 min by the infrared thermographic camera.

After treatment, sterile paper points were placed into the gingival sulcus of the maxillary second molars for 30 s and placed in 1.5 mL of sterilized PBS. Then, 10 μL of bacterial suspension was inoculated into 990 μL of FAB. After 48 h of anaerobic culture at 37 °C, the bacterial spread plate method was applied to evaluate the antibacterial efficacy in vivo.

Then, all rats were euthanized. The maxillary alveolar bone was fixed with 4% paraformaldehyde. For micro-CT analysis, samples were scanned using a CT imaging system (Milab, the Netherlands) and ABL/RL and BV/TV were calculated, while Tb.Th and Tb.Sp were measured.

For histological evaluation, samples were decalcified, embedded in paraffin, and cut into slices. Then, H&E staining, Masson's trichrome staining, and IHC staining of IL-6 (1∶200; Abcam, ab290735, UK) and Caspase-1 (1∶400; Proteintech, 22915-1-AP, USA) were performed. All sections were observed using an upright optical microscope (Olympus). H&E staining of vital viscera including the heart, liver, spleen, lungs, and kidneys was carried out to evaluate the in vivo biosafety of US-RuNPs.

In another experiment, the retention of US-RuNPs in the periodontal pockets was investigated. After treatment with 40 μg/mL of US-RuNPs solution, sterile paper points were placed into the periodontal pockets for 30 s and placed in 1.5 mL of deionized water at 12, 24, 36, 48, and 72 h. The concentration of US-RuNPs was then detected by ICP-MS.

$$\text{US-RuNPs Retention} = C_{\text{Time}}/40 \times 100\%,$$

where C_{Time} represents the concentration of US-RuNPs at each time.

5.13 Statistical analysis

Quantitative data from ⩾3 independent experiments were reported as mean±standard deviation. A one-way analysis of variance with Tukey's post-hoc test was used for statistical analysis using GraphPad Prism 8.0.2. $P<0.05$ was considered statistically significant ($^{*}P<0.05$, $^{**}P<0.01$, $^{***}P<0.001$).

Supplementary Information The online version contains supplementary material available at https://doi.org/10.1631/bdm.2400436.

Acknowledgements This work was supported by the National Key Research and Development Program of China (No. 2023YFB3813000), the National Natural Science Foundation of China (Nos. 82071085, 82020108011, and 82122014), and the Zhejiang Provincial Natural Science Foundation of China (No. LR21H140001). We thank Yanwei Li, Guifeng Xiao, Wei Yin, Zhaoxiaonan Lin, Xiaoli Hong, and Chao Bi from Core Facilities, Zhejiang University School of Medicine for their technical support. We thank Dandan Song and Guizhen Zhu at the Center of Cryo-Electron Microscopy (CCEM), Zhejiang University for their technical assistance with scanning electron microscopy.

Author contributions Conceptualization: DQY, DSL, FYL, and MFY. Data curation: YJS and PPX. Formal analysis: YJS, SBL, PHL, XYH, and MHX. Funding acquisition: MFY. Investigation: YJS, PPX, MJZ, and ZYQ. Methodology: YJS, PPX, MJZ, BZ, and ZCL. Project administration: DQY, FYL, and MFY. Resources: SBL, MJZ, and FYL. Software: BZ, ZCL, CYZ, and YX. Supervision: DSL and MFY. Validation: DQY, ZYQ, and PHL. Writing—original draft: YJS and PPX. Writing—review and editing: DQY, DSL, and MFY.

Declarations

Conflict of interest MFY is an associate editor for *Bio-Design and Manufacturing* and was not involved in the editorial review or the decision to publish this article. The authors declare that they have no conflict of interest.

Ethical approval All animal experiments have been approved by the Institutional Animal Care and Use Committee of Zhejiang University (approval number: ZJU20240084). All institutional and national guidelines for the care and use of laboratory animals were followed.

Data availability The data that support the findings of this study are available from the corresponding authors upon reasonable request.

References

1. Hajishengallis G, Chavakis T, Lambris JD (2020) Current understanding of periodontal disease pathogenesis and targets for host-modulation therapy. Periodontol 2000 84(1):14–34. https://doi.org/10.1111/prd.12331
2. Passanezi E, Sant'Ana ACP (2019) Role of occlusion in periodontal disease. Periodontol 2000 79(1):129–150. https://doi.org/10.1111/prd.12251
3. Janakiram C, Dye BA (2020) A public health approach for prevention of periodontal disease. Periodontol 2000 84(1):202–214. https://doi.org/10.1111/prd.12337
4. Pink C, Holtfreter B, Völzke H et al (2023) Periodontitis and systemic inflammation as independent and interacting risk

factors for mortality: evidence from a prospective cohort study. BMC Med 21(1):430. https://doi.org/10.1186/s12916-023-03139-4

5. Minty M, Canceil T, Serino M et al (2019) Oral microbiota-induced periodontitis: a new risk factor of metabolic diseases. Rev Endocr Metab Disord 20(4):449–459. https://doi.org/10.1007/s11154-019-09526-8
6. Li J, Song S, Meng JS et al (2021) 2D MOF periodontitis photodynamic ion therapy. J Am Chem Soc 143(37):15427–15439. https://doi.org/10.1021/jacs.1c07875
7. Song BQ, Xian WP, Sun Y et al (2023) *Akkermansia muciniphila* inhibited the periodontitis caused by *Fusobacterium nucleatum*. npj Biofilms Microbiomes 9(1):49. https://doi.org/10.1038/s41522-023-00417-0
8. El-Awady A, de Sousa Rabelo M, Meghil MM et al (2019) Polymicrobial synergy within oral biofilm promotes invasion of dendritic cells and survival of consortia members. npj Biofilms Microbiomes 5(1):11. https://doi.org/10.1038/s41522-019-0084-7
9. Tong F, Wang P, Chen ZQ et al (2023) Combined ferromagnetic nanoparticles for effective periodontal biofilm eradication in rat model. Int J Nanomed 18:2371–2388. https://doi.org/10.2147/IJN.S402410
10. Tuganbaev T, Yoshida K, Honda K (2022) The effects of oral microbiota on health. Science 376(6596):934–936. https://doi.org/10.1126/science.abn1890
11. Peng X, Cheng L, You Y et al (2022) Oral microbiota in human systematic diseases. Int J Oral Sci 14(1):14. https://doi.org/10.1038/s41368-022-00163-7
12. Qi F, Huang HF, Wang M et al (2022) Applications of antioxidants in dental procedures. Antioxidants 11(12):2492. https://doi.org/10.3390/antiox11122492
13. Buranasin P, Kominato H, Mizutani K et al (2023) Influence of reactive oxygen species on wound healing and tissue regeneration in periodontal and peri-implant tissues in diabetic patients. Antioxidants 12(9):1787. https://doi.org/10.3390/antiox12091787
14. Picciolo G, Mannino F, Irrera N et al (2022) Reduction of oxidative stress blunts the NLRP3 inflammatory cascade in LPS stimulated human gingival fibroblasts and oral mucosal epithelial cells. Biomed Pharmacother 146:112525. https://doi.org/10.1016/j.biopha.2021.112525
15. Pan WY, Wang QX, Chen QM (2019) The cytokine network involved in the host immune response to periodontitis. Int J Oral Sci 11(3):30. https://doi.org/10.1038/s41368-019-0064-z
16. Liu X, Li H (2022) A systematic review and meta-analysis on multiple cytokine gene polymorphisms in the pathogenesis of periodontitis. Front Immunol 12:713198. https://doi.org/10.3389/fimmu.2021.713198
17. Ren BJ, Lu JY, Li MH et al (2021) Anti-inflammatory effect of IL-1ra-loaded dextran/PLGA microspheres on *Porphyromonas gingivalis* lipopolysaccharide-stimulated macrophages in vitro and in vivo in a rat model of periodontitis. Biomed Pharmacother 134:111171. https://doi.org/10.1016/j.biopha.2020.111171
18. Chen K, Qiu PC, Yuan Y et al (2019) Pseurotin A inhibits osteoclastogenesis and prevents ovariectomized-induced bone loss by suppressing reactive oxygen species. Theranostics 9(6):1634–1650. https://doi.org/10.7150/thno.30206
19. Chen K, Liu YH, He JB et al (2020) Steroid-induced osteonecrosis of the femoral head reveals enhanced reactive oxygen species and hyperactive osteoclasts. Int J Biol Sci 16(11):1888–1900. https://doi.org/10.7150/ijbs.40917
20. Citterio F, Gualini G, Chang M et al (2022) Pocket closure and residual pockets after non-surgical periodontal therapy: a systematic review and meta-analysis. J Clin Periodontol 49(1):2–14. https://doi.org/10.1111/jcpe.13547
21. Tomasi C, Abrahamsson KH, Apatzidou D (2023) Subgingival instrumentation. Periodontol 2000 (early access). https://doi.org/10.1111/prd.12485
22. Shi EY, Bai LY, Mao LJ et al (2021) Self-assembled nanoparticles containing photosensitizer and polycationic brush for synergistic photothermal and photodynamic therapy against periodontitis. J Nanobiotechnol 19(1):413. https://doi.org/10.1186/s12951-021-01114-w
23. Bao XF, Zhao JH, Sun J et al (2018) Polydopamine nanoparticles as efficient scavengers for reactive oxygen species in periodontal disease. ACS Nano 12(9):8882–8892. https://doi.org/10.1021/acsnano.8b04022
24. Chen EN, Wang TY, Tu Y et al (2023) ROS-scavenging biomaterials for periodontitis. J Mater Chem B 11(3):482–499. https://doi.org/10.1039/d2tb02319a
25. Wang Y, Li CY, Wan Y et al (2021) Quercetin-loaded ceria nanocomposite potentiate dual-directional immunoregulation via macrophage polarization against periodontal inflammation. Small 17(41):e2101505. https://doi.org/10.1002/smll.202101505
26. Yu YJ, Zhao S, Gu DA et al (2022) Cerium oxide nanozyme attenuates periodontal bone destruction by inhibiting the ROS-NFκB pathway. Nanoscale 14(7):2628–2637. https://doi.org/10.1039/d1nr06043k
27. Phan-Xuan T, Breitung B, Dailey LA (2024) Nanozymes for biomedical applications: multi-metallic systems may improve activity but at the cost of higher toxicity? Wiley Interdiscip Rev Nanomed Nanobiotechnol 16(4):e1981. https://doi.org/10.1002/wnan.1981
28. Singh A, Barman P (2021) Recent advances in Schiff base ruthenium metal complexes: synthesis and applications. Top Curr Chem 379(4):29. https://doi.org/10.1007/s41061-021-00342-w
29. Maikoo S, Makayane D, Booysen IN et al (2021) Ruthenium compounds as potential therapeutic agents for type 2 diabetes mellitus. Eur J Med Chem 213:113064. https://doi.org/10.1016/j.ejmech.2020.113064
30. Liu Z, Xie LN, Qiu KQ et al (2020) An ultrasmall RuO_2 nanozyme exhibiting multienzyme-like activity for the prevention of acute kidney injury. ACS Appl Mater Interfaces 12(28):31205–31216. https://doi.org/10.1021/acsami.0c07886
31. Bai Q, Han YP, Khan S et al (2024) A novel endoplasmic reticulum-targeted metal-organic framework-confined ruthenium (Ru) nanozyme regulation of oxidative stress for central post-stroke pain. Adv Healthc Mater 13(2):e2302526. https://doi.org/10.1002/adhm.202302526
32. Wu CY, Han XG, Feng W et al (2021) Multi-enzymatic activities of ultrasmall ruthenium oxide for anti-inflammation and neuroprotection. Chem Eng J 411:128543. https://doi.org/10.1016/j.cej.2021.128543
33. Huang XQ, Chen GJ, Pan JL et al (2016) Effective PDT/PTT dual-modal phototherapeutic killing of pathogenic bacteria by using ruthenium nanoparticles. J Mater Chem B 4(37):6258–6270. https://doi.org/10.1039/c6tb01122e
34. Liu YN, Lin AG, Liu JW et al (2019) Enzyme-responsive mesoporous ruthenium for combined chemo-photothermal therapy of drug-resistant bacteria. ACS Appl Mater Interfaces 11(30): 26590–26606. https://doi.org/10.1021/acsami.9b07866
35. Zhu XF, Chen X, Jia Z et al (2021) Cationic chitosan@Ruthenium dioxide hybrid nanozymes for photothermal therapy enhancing ROS-mediated eradicating multidrug resistant bacterial infection. J Colloid Interface Sci 603:615–632. https://doi.org/10.1016/j.jcis.2021.06.073
36. Nasiri K, Masoumi SM, Amini S et al (2023) Recent advances in metal nanoparticles to treat periodontitis. J Nanobiotechnol

21(1):283.
https://doi.org/10.1186/s12951-023-02042-7

37. Lu H, Ni SQ (2024) Review on sterilization techniques, and the application potential of phage lyase and lyase immobilization in fighting drug-resistant bacteria. J Mater Chem B 12(14):3317–3335.
https://doi.org/10.1039/d3tb02366d
38. Cui FC, Li TT, Wang DF et al (2022) Recent advances in carbon-based nanomaterials for combating bacterial biofilm-associated infections. J Hazard Mater 431:128597.
https://doi.org/10.1016/j.jhazmat.2022.128597
39. Chen Y, Gao YJ, Chen Y et al (2020) Nanomaterials-based photothermal therapy and its potentials in antibacterial treatment. J Contr Release 328:251–262.
https://doi.org/10.1016/j.jconrel.2020.08.055
40. Ding QY, Sun TF, Su WJ et al (2022) Bioinspired multifunctional black phosphorus hydrogel with antibacterial and antioxidant properties: a stepwise countermeasure for diabetic skin wound healing. Adv Healthc Mater 11(12):2102791.
https://doi.org/10.1002/adhm.202102791
41. Liu XY, Li RF, Jia J et al (2024) Antibacterial micro/nanomotors: current research progress, challenges, and opportunities. Theranostics 14(3):1029–1048.
https://doi.org/10.7150/thno.92449
42. Li XY, Coulter Montague E, Pollinzi A et al (2022) Design of smart size-, surface-, and shape-switching nanoparticles to improve therapeutic efficacy. Small 18(6):e2104632.
https://doi.org/10.1002/smll.202104632
43. Öztürk K, Kaplan M, Çalış S (2024) Effects of nanoparticle size, shape, and zeta potential on drug delivery. Int J Pharm 666: 124799.
https://doi.org/10.1016/j.ijpharm.2024.124799
44. Xu JQ, Song MD, Fang Z et al (2023) Applications and challenges of ultra-small particle size nanoparticles in tumor therapy. J Contr Release 353:699–712.
https://doi.org/10.1016/j.jconrel.2022.12.028
45. Chang BS, Zhang LQ, Wu SL et al (2022) Engineering single-atom catalysts toward biomedical applications. Chem Soc Rev 51(9):3688–3734.
https://doi.org/10.1039/d1cs00421b
46. Balta MG, Papathanasiou E, Blix IJ et al (2021) Host modulation and treatment of periodontal disease. J Dent Res 100(8): 798–809.
https://doi.org/10.1177/0022034521995157
47. Guo JX, Wei WY, Zhao YN et al (2022) Iron oxide nanoparticles with photothermal performance and enhanced nanozyme activity for bacteria-infected wound therapy. Regen Biomater 9: rbac041.
https://doi.org/10.1093/rb/rbac041
48. Cen JQ, Huang YQ, Liu J et al (2022) Thermo-responsive palladium-ruthenium nanozyme synergistic photodynamic therapy for metastatic breast cancer management. J Mater Chem B 10(48):10027–10041.
https://doi.org/10.1039/d2tb01481e
49. Deng XX, Liu XB, Wu S et al (2021) Ratiometric fluorescence imaging of intracellular microRNA with NIR-assisted signal amplification by a Ru-SiO_2@polydopamine nanoplatform. ACS Appl Mater Interfaces 13(38):45214–45223.
https://doi.org/10.1021/acsami.1c11324
50. Pedrosa TL, Farooq S, de Araujo RE (2022) Selecting high-performance gold nanorods for photothermal conversion. Nanomaterials 12(23):4188.
https://doi.org/10.3390/nano12234188
51. Cai YY, Choi YC, Kagan CR (2023) Chemical and physical properties of photonic noble-metal nanomaterials. Adv Mater 35(34):e2108104.
https://doi.org/10.1002/adma.202108104
52. Jauffred L, Samadi A, Klingberg H et al (2019) Plasmonic heating of nanostructures. Chem Rev 119(13):8087–8130.
https://doi.org/10.1021/acs.chemrev.8b00738
53. Xin Y, Yu KF, Zhang LT et al (2021) Copper-based plasmonic catalysis: recent advances and future perspectives. Adv Mater 33(32):2008145.
https://doi.org/10.1002/adma.202008145
54. Li P, Chen Z, Xia F et al (2023) Leveraging coupling effect-enhanced surface plasmon resonance of ruthenium nanocrystal-decorated mesoporous silica nanoparticles for boosted photothermal immunotherapy. Adv Healthc Mater 12(31):e2302111.
https://doi.org/10.1002/adhm.202302111
55. Robert A, Meunier B (2022) How to define a nanozyme. ACS Nano 16(5):6956–6959.
https://doi.org/10.1021/acsnano.2c02966
56. Wang MZ, Zhang JX, Wei JY et al (2024) Phage-inspired strategies to combat antibacterial resistance. Crit Rev Microbiol 50(2): 196–211.
https://doi.org/10.1080/1040841X.2023.2181056
57. Chen Z, Yu YX, Gao YH et al (2023) Rational design strategies for nanozymes. ACS Nano 17(14):13062–13080.
https://doi.org/10.1021/acsnano.3c04378
58. Ding XT, Zhao Z, Zhang YF et al (2023) Activity regulating strategies of nanozymes for biomedical applications. Small 19(11): 2207142.
https://doi.org/10.1002/smll.202207142
59. Xia F, Hu X, Zhang B et al (2022) Ultrasmall ruthenium nanoparticles with boosted antioxidant activity upregulate regulatory T cells for highly efficient liver injury therapy. Small 18(29): e2201558.
https://doi.org/10.1002/smll.202201558
60. Sczepanik FSC, Grossi ML, Casati M et al (2020) Periodontitis is an inflammatory disease of oxidative stress: we should treat it that way. Periodontol 2000 84(1):45–68.
https://doi.org/10.1111/prd.12342
61. Xu YY, Luo YF, Weng ZZ et al (2023) Microenvironment-responsive metal-phenolic nanozyme release platform with antibacterial, ROS scavenging, and osteogenesis for periodontitis. ACS Nano 17(19):18732–18746.
https://doi.org/10.1021/acsnano.3c01940
62. Bosshardt DD (2018) The periodontal pocket: pathogenesis, histopathology and consequences. Periodontol 2000 76(1):43–50.
https://doi.org/10.1111/prd.12153
63. Rajeshwari HR, Dinesh D, Satveer J et al (2019) Local drug delivery systems in the management of periodontitis: a scientific review. J Contr Release 307:393–409.
https://doi.org/10.1016/j.jconrel.2019.06.038
64. Xu MZ, Qi YM, Liu GS et al (2023) Size-dependent in vivo transport of nanoparticles: implications for delivery, targeting, and clearance. ACS Nano 17(21):20825–20849.
https://doi.org/10.1021/acsnano.3c05853
65. Yu N, Huang L, Zhou YB et al (2019) Near-infrared-light activatable nanoparticles for deep-tissue-penetrating wireless optogenetics. Adv Healthc Mater 8(6):1801132.
https://doi.org/10.1002/adhm.201801132
66. Yang Y, Jiang QY, Zhang F (2024) Nanocrystals for deep-tissue in vivo luminescence imaging in the near-infrared region. Chem Rev 124(2):554–628.
https://doi.org/10.1021/acs.chemrev.3c00506
67. Kang Y, Xu LL, Dong JR et al (2024) Programmed microalgae-gel promotes chronic wound healing in diabetes. Nat Commun 15(1):1042.
https://doi.org/10.1038/s41467-024-45101-9